**Neuron, Volume *91***

## Supplemental Information

# Actin- and Myosin-Dependent Vesicle Loading of Presynaptic Docking Sites Prior to Exocytosis

**Takafumi Miki, Gerardo Malagon, Camila Pulido, Isabel Llano, Erwin Neher, and Alain Marty**

**Supplemental Information**

**Inventory of Supplemental Information**

Supplemental Information contains 7 Supplemental Figures, followed by Supplemental Experimental Procedures, and by Supplemental References.

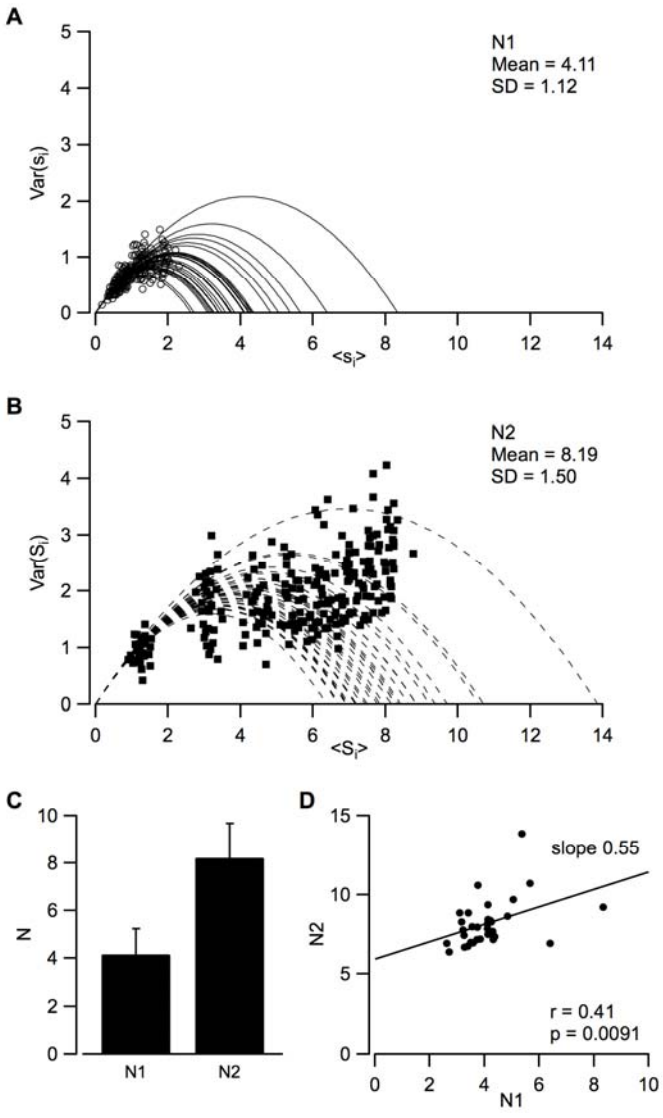


**Figure S1, related to Figures 1 and 2: Stochastic uncertainty on the determination of $N_1$ and $N_2$**
Monte Carlo simulations were performed mimicking 30-trial experiments with $N_1 = 4$, $N_2 = 8$ (renewable 2-step model giving the best least-squares score for control data: $\delta = 0.45$, $p = 0.7$, $r = 0.6$, $s = 0.15$).
**A, B**: In each simulated experiment, $N_1$ and $N_2$ were obtained from parabolic fits to synchronized (A: circles, simulated variance/mean points for individual stimulations; continuous lines, corresponding parabolic fits) and cumulative (B: squares and dotted lines) variance plots.
**C**: Mean and SD of $N_1$ and $N_2$ values resulting from individual simulations.
**D**: Plot of $N_2$ vs. $N_1$ in individual simulations reveals a significant correlation. This results from the link between $s_i$ and $S_i$ values in individual trials: large $s_i$ values (generated by stochastic fluctuations) tend to yield both large $N_1$ and large $N_2$ estimates. However the corresponding Pearson's coefficient ($r = 0.41$), as well as the slope of the regression line (0.55), are markedly weaker than experimentally observed (respectively 0.81 and 1.63; Fig. 1H).
Overall the present analysis suggests that part of the variations of $N_1$ and $N_2$ determined in individual experiments arise from statistical fluctuations linked to the finite number of trials that were recorded (usually 30). However the finding of larger values for Pearson's coefficient, as well as for the slope of the regression line, in Fig. 1H (experimental) compared with panel D (simulations), suggests that the observed correlation between $N_1$ and $N_2$ exceeds the correlation expected from statistical fluctuations, and mainly originates from genuine differences among simple synapses.

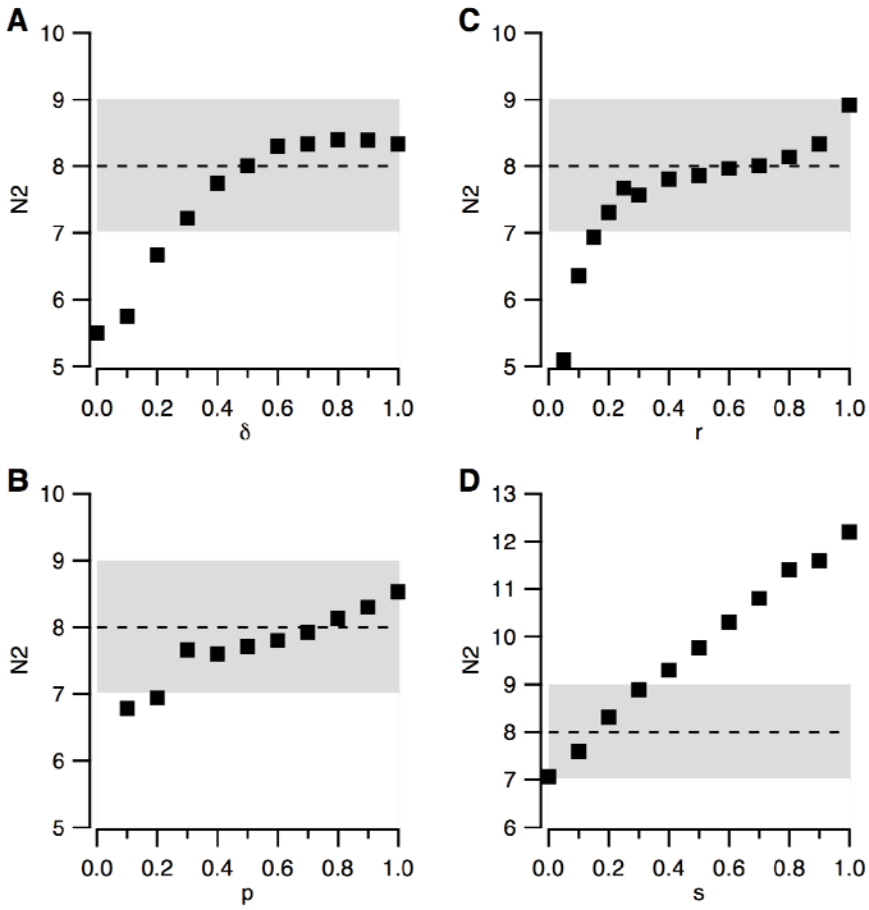


**Figure S2, related to Figure 2: Effect of varying δ, p, r or s on estimate of $N_2$**
Monte Carlo simulations were run as in Fig. 2E, based on the renewable 2-step model giving the best least-squares score for control data: δ = 0.45, p = 0.7, r = 0.6, s = 0.15. 3 of the parameters were kept identical to this reference case, and the 4th parameter was altered between 0 and 1. For each new value of the altered parameter the corresponding value of $N_2$ was determined by using the parabolic plot of cumulative variance. In each plot a band indicates a range of $N_2$ values ($7 \leq N_2 \leq 9$) considered reasonably close to the ideal value $N_2 = 8$.
**A**: The condition ($7 \leq N_2 \leq 9$) was fulfilled for δ values ranging from 0.3 to 1.
**B**: The condition ($7 \leq N_2 \leq 9$) was fulfilled for p values ranging from 0.3 to 1.
**C**: The condition ($7 \leq N_2 \leq 9$) was fulfilled for r values ranging from 0.2 to 1.
**D**: The condition ($7 \leq N_2 \leq 9$) was fulfilled for s values ranging from 0 to 0.3.

These plots show that approximately correct $N_2$ values are obtained for large ranges of model parameters. However large deviations are predicted for very low δ or r values, as well as for s values larger than 0.3.

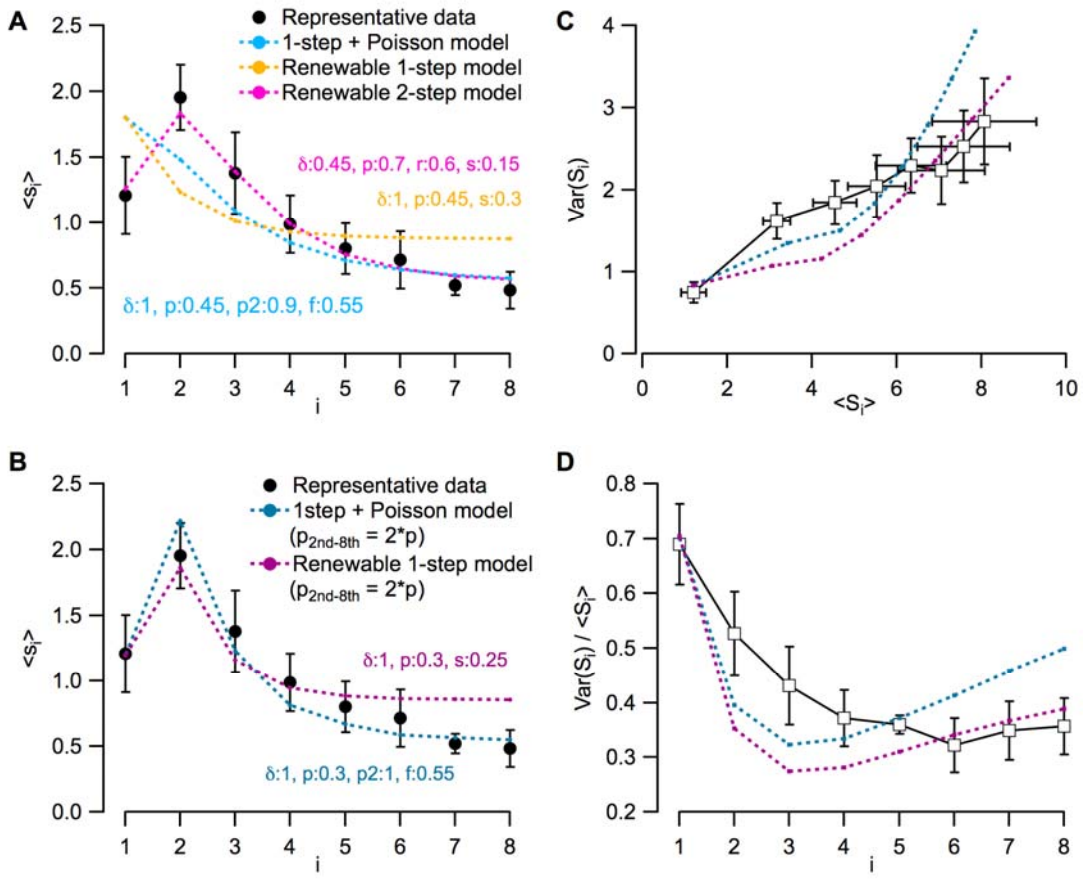


**Figure S3, related to Figure 2: Simulation of 1-step models with variable p values**
**A:** $\langle s_i \rangle$ curves corresponding to the best parameter sets from Fig. 2F, for the 2-step model (red), for the 1-step + Poisson model (blue), and for the renewable 1-step model (orange), are compared to experimental data (black). Here p is constant for all models, and only the 2-step model approaches the data.
**B-D:** After imposing a 2-fold ratio for p between the first and the second stimulus ($p_i/p_1 = 2$ for i = 2-8), $\langle s_i \rangle$ curves for the 2 variants of the 1-step model become closer to experimental data (**B**). However, even after readjustment of the parameter sets to minimize summed squared deviations, both 1-step models fail to account for the experimental var ($S_i$) curve (**C**) or for the var ($S_i$) / $\langle S_i \rangle$ curve (**D**).

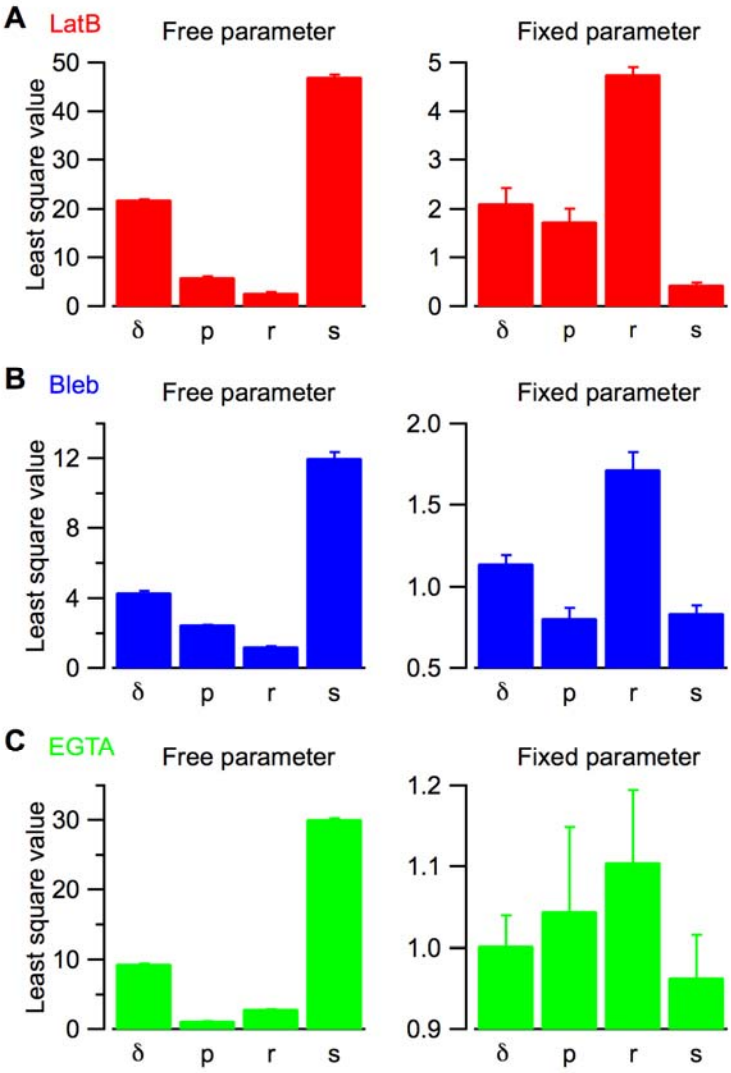


**Figure S4, related to Figure 5: Least-squares scores of simulations of experiments with latrunculin B, blebbistatin and EGTA**

The reference simulation is the 2-step model of Fig. 2E with the set of parameters giving the best least-squares score for control data: $\delta = 0.45$, $p = 0.7$, $r = 0.6$, $s = 0.15$. Left column: Starting with these values, simulations of var ($S_i$) curves were run keeping 3 parameters fixed at these control values and leaving 1 free. The least-squares score is then plotted as a function of the parameter that is varied. Right column: Simulations were now run keeping 1 parameter fixed and leaving 3 free. The least-squares score is then plotted as a function of the parameter that is fixed. Low scores in the left column, and/or high scores in the right column, indicate that changing the corresponding parameter is important in achieving a good model of the examined pharmacological effect.

**A:** Latrunculin B experiments. r gives the lowest score in the free parameter test (left), and the highest score in the fixed parameter test (right). This indicates that a change in r is the principal factor determining the effects of latrunculin B.

**B:** Blebbistatin experiments. Again r appears as the principal parameter determining the effects of blebbistatin.

**C:** EGTA experiments. Changes in parameters p and r contribute strongly to determine the effects of EGTA, while parameters δ and s appear less important.

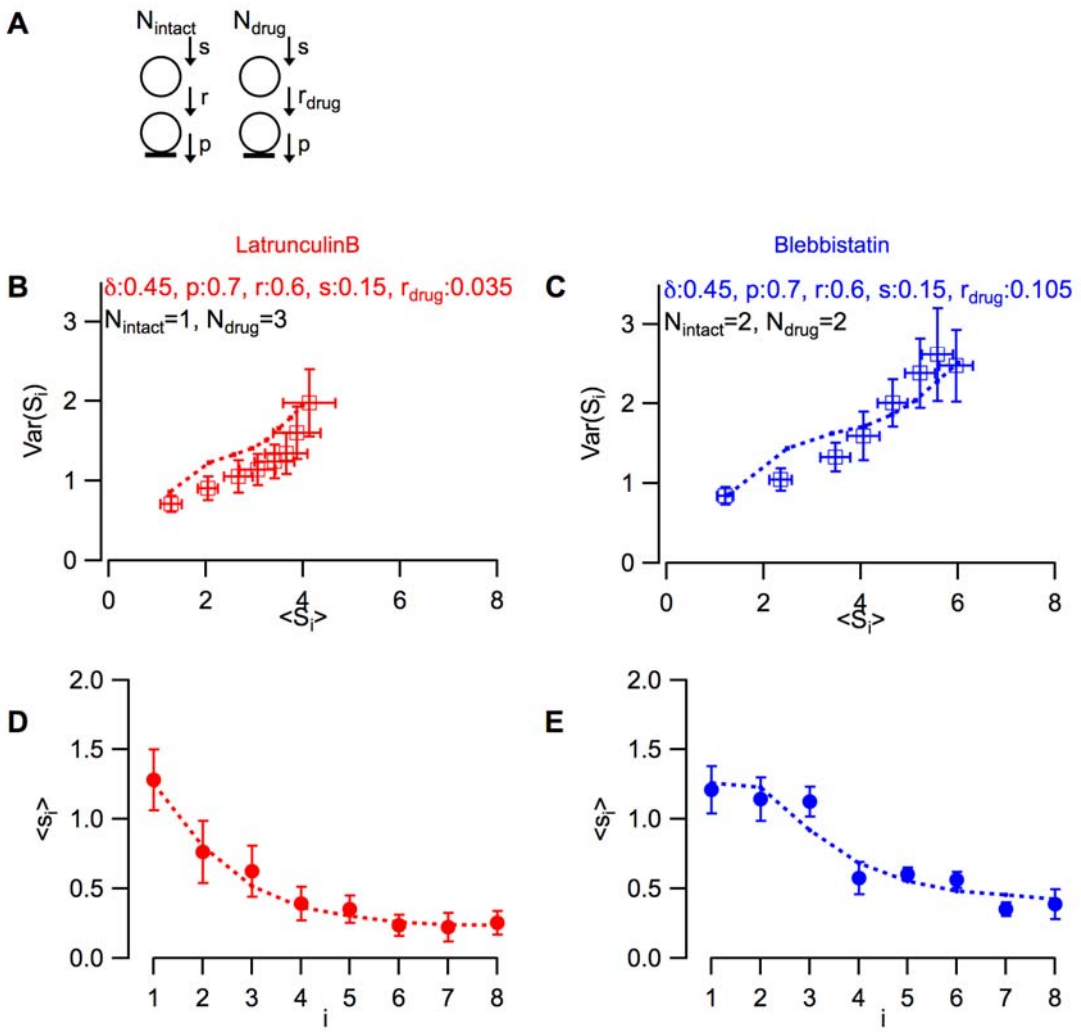


**Figure S5, related to Figure 6: Simulation of heterogeneous latrunculin B and blebbistatin effects**
**A:** Here we assume that some of the docking sites continue to operate normally ($N_{intact}$ = 1 in latrunculin B, and $N_{intact}$ = 2 in blebbistatin), while the other docking sites have a much reduced r value (0.035 in latrunculin, and 0.105 in blebbistatin).
**B, C:** var ($S_i$) vs. $<S_i>$ curves in latrunculin B and in blebbistatin (squares: grouped data; dashed lines: simulations). Fits are closer to experimental data than in Fig. 6B.
**D, E:** Same for $<s_i>$ curves.

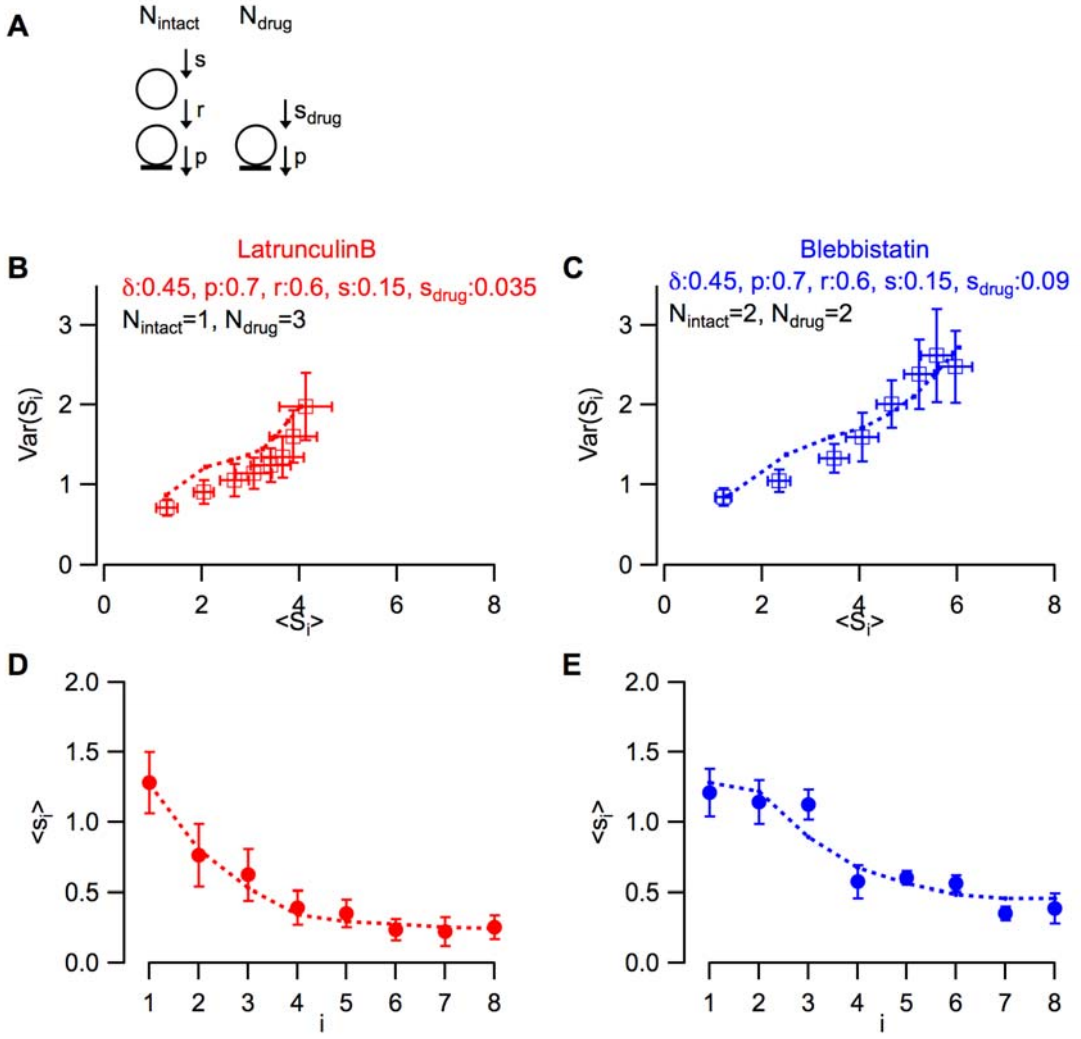


**Figure S6, related to Figure 6: Simulation of latrunculin B experiments and of blebbistatin experiments, assuming an elimination of replacement sites**

**A:** In these simulations, like in Fig. S5, some docking sites remain intact during parmacological treatment (1 in latrunculin B, 2 in blebbistatin). Other docking sites lose their associated replacement site, and are directly replenished from a large vesicular pool with a new rate constant $s_{drug}$, smaller than s.

**B, C:** Least-squares fits of var ($S_i$) vs. $<S_i>$ curves in latrunculin B and in blebbistatin respectively gave $s_{drug}$ = 0.035 (**B**) and $s_{drug}$ = 0.09 (**C**).

**D, E:** Corresponding $<s_i>$ curves are close to experimental data.

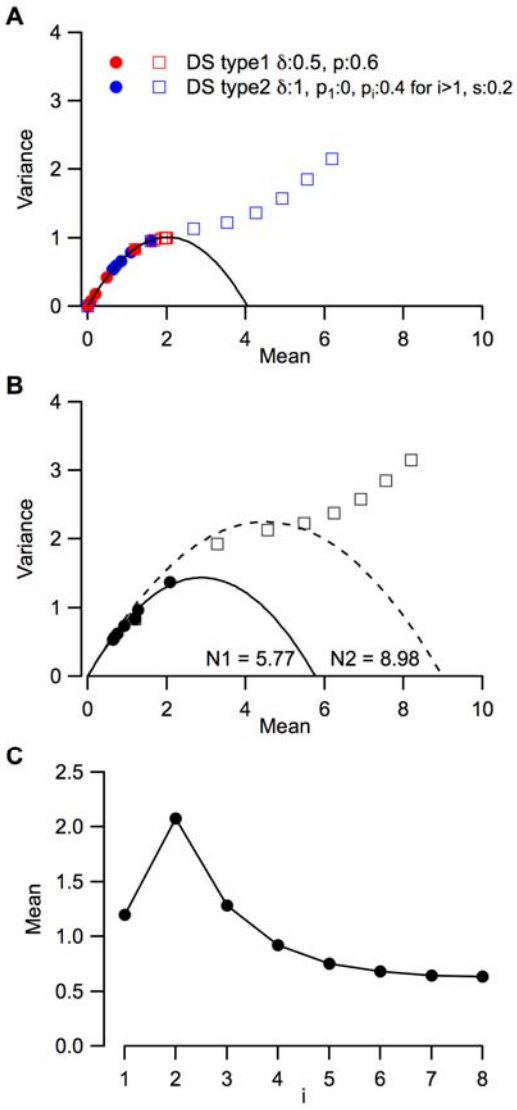


**Figure S7, related to Figure 6: Simulation of two different populations of docking sites**
In this simulation two sets of docking sites are assumed to coexist in the same active zone. First, 4 docking sites follow a 1-step docking site model without replenishment. They primarily contribute to the responses observed in the beginning of the train, particularly in response to the 1st and 2nd stimuli. A second set of 4 docking sites follow a 1-step docking site model with replenishment. These docking sites are assumed to be totally silent in response to the 1st stimulus, and to be turned on with a fixed p value starting with the 2nd stimulus. They primarily account for late responses in the train. Even though this model produces plots for var ($s_i$), var ($S_i$) and $<s_i>$ plots that are similar to experimental data, it is less attractive than the 2-step model for two reasons. First, the present model assumes an abrupt shift from one set of docking sites to the other. This sudden shift is necessary for the model to work (or else the var ($s_i$) curve would deviate from the experimental data), but it does not have any simple mechanistic interpretation and is therefore unlikely. Secondly, the present model does not account readily for the latrunculin B/blebbistatin results.
**A**: Separate var ($s_i$) plots (circles) and var ($S_i$) plots (squares) for the two sets of docking sites (red: without replenishment; blue: with replenishment).
**B**: Simulation of var ($s_i$) plots (circles) and var ($S_i$) plots (squares) for the combination of the two sets of docking sites. Some of the var ($s_i$) points deviate from the $N_1$= 4 parabola, but overall the var ($s_i$) curve can be reasonably well fitted with a parabola with $N_1$= 5.77 (circles and associated continuous parabola). Meanwhile the var ($S_i$) plot can be approached with a parabola giving $N_2$= 8.98 (squares and associated dashed parabola). Note similarity with group data of Fig. 5D.
**C**: $<s_i>$ plot for the same simulation, similar to the experimental results of Fig. 6A.

**Supplemental Experimental Procedures**

**Recording procedures**

Sagittal slices (200 μm thick) were prepared from the cerebellar vermis of Sprague Dawley rats (PN 13-16) following the animal care guidelines of our host institution (approval number A-750607). Procedures to record from MLIs were as described (Llano and Gerschenfeld, 1993). About 2/3 of the recordings were from basket cells, defined as MLIs located in the proximal third of the molecular layer, and the remaining 1/3 were stellate cells. This percentage applied both to control data and to data obtained with a pharmacological manipulation (latruncullin B, blebbistatin, or EGTA AM). The composition of the standard extracellular solution was (in mM): 130 NaCl, 2.5 KCl, 26 $NaHCO_3$, 1.3 $NaH_2PO_4$, 10 glucose, 2 $CaCl_2$, and 1 $MgCl_2$; osmolarity: 300 mosm/l). This solution was equilibrated with 95 % $O_2$ and 5 % $CO_2$ (pH 7.4). The standard internal recording solution contained (in mM): 144 K-glutamate, 6 KCl, 4.6 $MgCl_2$, 1 EGTA, 0.1 $CaCl_2$,10 HEPES-K, 4 ATP-Na, 0.4 GTP-Na; pH 7.3; osmolarity: 300 mosm. Alexa 488 was included in this solution to visualize the dendritic tree. Recordings were at 30-34 $^oC$.

**Extracellular stimulation and recording of single synapses**

MLIs were recorded under voltage clamp at -60 mV. After allowing diffusion of the Alexa dye for a few minutes the outline of the dendritic tree was outlined using a CCD camera. For extracellular stimulation a theta-glass pipette was filled with a solution containing (in mM): 145 Na Cl, 2.5 KCl, 2 $CaCl_2$, 1 $MgCl_2$, 10 HEPES-Na, at a pH of 7.3. The extracellular solution was switched to a new solution containing 3 mM external calcium in order to enhance release probability. NMDA receptors and $GABA_A$ receptors were blocked by inclusion of APV (50 μM) and gabazine (15 μM). The tip of the stimulation pipette was positioned on top of a dendrite, at the slice surface. Once a response was found the stimulation threshold was determined, and the position of the pipette was changed to minimize that threshold. During recording, amplitudes of late events were visually inspected, and if these amplitudes appeared heterogeneous, the corresponding stimulation site was abandoned. Definitive acceptance of the experiment as a usable single synapse recording occurred after analysis and depended on 3 criteria (Malagon et al., 2016): (1) a decrement of EPSC amplitudes of second events in a pair, reflecting sharing a common set of receptors belonging to one postsynaptic receptor density; (2) a Gaussian distribution of EPSC amplitudes with a CV less than 0.5; (3) stability of the overall responsiveness over time. PSCs were elicited by voltage steps of 10-30 V (0.1 ms duration). Trains of 8 such pulses (interstimulus interval: 5 ms) were applied repetitively, with intervals of 15 s between trains. Statistical data were derived from sequences of 10-30 trains.

**Detection of PSCs during trains**

The recorded traces were analyzed using Igor (Wavemetrics, Lake Oswego, USA). Isolated, presumably quantal EPSCs were selected in the late part of the response, aligned with respect to the rising phase, and averaged. The averaged quantal EPSC was fitted with the sum of 3 exponential functions, one for the rising phase and two for the decay. The model quantal EPSC waveform was used to deconvolve the original traces. The deconvolution of the model quantal EPSC was a short transient (called 'spike') and the deconvolution of entire traces were decomposed as the sum of several spikes after adjustment of their amplitudes and times of occurrence. This created a table of evoked EPSCs, each characterized by its time of occurrence and its amplitude. Corrections were applied to account for undetected double EPSCs (estimated temporal separation necessary for detection of individual events, 0.2 ms: Malagon et al., 2016). Temperature plots displayed the estimated numbers of EPSCs for each 5 ms period following individual stimuli, where 'hot' colors feature large vesicle numbers, and failures appear in deep blue (examples in Figs. 1A-B).

**Calcium imaging of presynaptic varicosities**

Sagittal (200 μm) or transverse (350 μm) slices from rats aged 13 to 15 days were prepared using a modified extracellular saline, as detailed in Brenowitz and Regehr (2007). Experiments were conducted at 32-34 $^oC$ with the 3 mM extracellular calcium saline used in the electrophysiology experiments. APV (50 μM) and gabazine (15 μM) were included. Granule cells were loaded under whole-cell recording with a solution containing (in mM): 140 K gluconate, 5.4 KCl, 4.1 $MgCl_2$, 9.9 HEPES-K, 0.36 Na-GTP, 3.6 Na-ATP, 500 μM of the calcium-sensitive indicator Oregon green 488 BAPTA-6F (OGB-6F; $K_d$ for calcium of 5.1 μM estimated from *in vitro* calibrations) and 20 μM Alexa-594. Both fluorophores were from Invitrogen. Imaging was performed with a custom-built 2-photon system based on the design of Tan et al. (1999), with 820 nm excitation provided by a MaiTai Ti-Sapphire laser (Spectra Physics, USA). In order to visualize the granule cell axon, large raster scans

were performed while acquiring the Alexa 594 fluorescence with a red channel photomultiplier (Hamamatsu H7422 PA-sel, bandpass emission filter 635±65 nm, Chroma Technology). Once a varicosity was identifed, OGB-6F signals were acquired with a green channel (bandpass filtered at 635 ± 65 nm, Chroma Technology; avalanche photodiode Perkin Elmer, SPCM-AQR-13) using raster scans of 5 by 2 µm dimensions at dwell times of 2 ms. The granule cells were kept under current clamp conditions with resting membrane potential around -85 to -95 mV. APs were evoked by 1 ms steps of 350-500 pA. Stimulation protocols alternated between 1, 2, 4 and 8 APs at 200 Hz and were repeated every 20 to 30 seconds. Calcium signaling was analyzed in the pixels encompassing the varicosity in terms of fluorescence changes relative to pre-stimulus values ($\Delta F/F_o$, expressed in %) with software written in the IGOR-Pro programming environment (Wavemetric, Lake Oswego, OR, USA). Averages were performed over 3-11 repetitions.

An 'in vitro' calibration of the dependence of OGB-6F fluorescence on calcium concentration was performed using a series of calcium buffers with high buffering capacity. It gave a ratio of 6.5 between the fluorescence $F_{max}$ at saturating calcium and the fluorescence $F_{0Ca}$ in the absence of calcium, and a $K_d$ of 5 µM. The hyperbolic curve in Fig. 3D (blue trace) corresponds to a linear dependence of the peak calcium concentration $Ca_i$ on AP number assuming $F_{max} / F_{0Ca} = 6.5$, and half saturation following 26 consecutive APs. $Ca_i$ was calculated by inverting the relation $F = F_{OCa} + (F_{max} - F_{OCa})\ Ca_i / (Ca_i + K_d)$ between observed fluorescence and calcium, giving an approximately linear relation on AP number (Fig. 3E). This calculation includes the basal calcium concentration $Ca_b$ as a free parameter. In the figure shown $Ca_b$ was chosen arbitrarily at 50 nM. In practice however, changing $Ca_b$ between 25 and 100 nM did not affect our conclusions, in the sense that the relation between $Ca_i$ and AP number remained linear, with a slope that changed over a small range (0.20 to 0.23 µM/AP). To correct this estimate of $Ca_i$ rise for the added buffering capacity of OGB-6F, we used the relation $Ca_{cor} = Ca_i\ (\kappa_o + \kappa_B)/\ \kappa_o$, where the intrinsic buffering capacity $\kappa_o$ was taken as 56, and the buffer capacity $\kappa_B$ was taken as 100 (Brenowitz and Regehr, 2007).

**Pharmacological manipulations**
Data were collected at least 5 min after switching the bath solution to latruncullin B or to blebbistatin, and 10 min after switching to EGTA-AM.

**Monte Carlo simulations**
We implemented 5 stochastic synaptic release models based on Monte Carlo simulations using Igor Pro (Wavemetric, Lake Oswego, OR, USA). In all of them, we assumed 4 independent docking sites, which were occupied by synaptic vesicles with a probability of δ before the 1st stimulation. When a vesicle is present at the site, release occurs with a probability of p. In some models, p is a changeable probability that depends on stimulus number (i). After releasing, if replenishment of the docking site is considered, it occurs stochastically with a constant rate R as long as the replacement site is occupied. Simulations proceeded with a time increment of 0.05 ms.

In the cases where a replacement site is assumed to precede the docking site state, occupancy probability of the replacement site is fixed at 1 before starting stimulations. After consumption of the vesicle, replenishment of the replacement site occurs stochastically with constant rate S, if such a replenishment step is considered ("renewable 2-step model").

In each stimulus, we computed the number and cumulative number of released vesicles. And we calculated mean, variance, and covariance for these two sets of parameters. To evaluate the likelihood of various models, we performed least square fits of cumulative variance-mean plots obtained from experimental data. For this fitting model parameters (δ, p, r, s) were incremented with intervals of 0.05.

**Statistical evaluation of group results**
Results of group data analysis are presented as mean ± s. e. m., or as regression lines. *n* values represent the number of independent experiments. When analyzing means, *p* values are based on Wilcoxon's rank test (either paired or unpaired). When analyzing ratios to control situation, *p* reflects the area of the normal distribution corresponding to the values of the mean and s. e. m. When analyzing correlations illustrated with regression lines, *r* represents Pearson's correlation coefficient, and *p* assesses the probability of correlation given the value of *r* and the number of degrees of freedom of the data.

**Supplemental References**

Brenowitz, S. D., and Regehr W. G. (2007). Reliability and heterogeneity of calcium signaling at single presynaptic boutons of cerebellar granule cells. J. Neurosci., 27, 7888-7898.

Llano, I., and Gerschenfeld, H. M. (1993). Inhibitory synaptic currents in stellate cells of rat cerebellar slices. J. Physiol. 468, 177-200.

Malagon, G., Miki, T., Llano, I., Neher, E. and Marty, A. (2016). Counting vesicular release events reveals binomial release statistics at single glutamatergic synapses. J. Neurosci. 36, 4010-4025.

Tan, Y. P., Llano, I., Hopt, A., Würrlehausen, F., and Neher, E. (1999). Fast scanning and efficient photodetection in a simple two-photon microscope. J. Neurosci. Methods, 92, 123-135.